Applied Catalysis B: Environmental 214 (2017) 78–88

Contents lists available at ScienceDirect

Applied Catalysis B: Environmental

journal homepage: www.elsevier.com/locate/apcatb

The influence of different Cu species onto multi-copper-contained hybrid materials' photocatalytic property and mechanism of chlorophenol degradation

Shengjie Xia[a,*], Xiaofeng Zhang[a], Xiaobo Zhou[b], Yue Meng[a,c], Jilong Xue[a], Zheming Ni[a,*]

[a] Department of Chemistry, College of Chemical Engineering, Zhejiang University of Technology, Hangzhou 310032, PR China
[b] Toxikon Corporation, 15 Wiggins Ave, Bedford, MA 01730, USA
[c] Department of Materials Chemistry, School of Life Science, Huzhou Teachers college, Huzhou 313000, PR China

ARTICLE INFO

Article history:
Received 15 March 2017
Received in revised form 3 May 2017
Accepted 9 May 2017
Available online 10 May 2017

Keywords:
Layered double hydroxides
Cu species
Photocatalysis
Chlorophenol (2,4,6-TCP)
Active free radicals

ABSTRACT

In this paper, we synthesized a series of novel layered double hydroxides (LDHs) based materials with different organic/inorganic Cu species ($Cu^3O/CuCr^1$–Cu^2/SB–LDHs). The Cu species were distributed in the layers (defined as Cu^1), intercalated between the layers (Cu^2) and combined on the surface of the material (Cu^3), respectively. The percentage of each Cu specie was adjusted to reveal the connection between different modifications and their photocatalytic activities as well as the modifications and the mechanism towards the chlorophenol (2,4,6-TCP) degradation. The experimental results showed that photodegradation of TCP varied due to different Cu species, the catalyst with the highest Cu concentration between the layers had the highest TCP degradation rate of 95.1%. In addition, the apparent quantum efficiency of different Cu^3O/Cu^1Cr–Cu^2/SB–LDH materials was at the range of 0.42% to 0.60%, which was higher than that of CuCr–LDHs (0.21%) and CuCr–CuSB–LDHs (0.32%). The free radical tests showed that different Cu species determined the generation of hydroxyl radical, super oxide free radical and peroxy radicals, differently. These three radicals contributed to 46.2%, 22.5% and 10.9%, respectively, for TCP degradation during the photocatalytic reaction. Therefore, it is critical to study the influence of different Cu modifications to the improvement of photocatalytic reactivity and selectivity of Cu^3O/Cu^1Cr–Cu^2/SB–LDH material. In addition, the intermediates, pathway and photoreaction mechanism of TCP degradation were also investigated in detail.

1. Introduction

Layered double hydroxides (LDHs) is a group of inorganic compounds composed of positively charged layers with anions distributed between the layers, as Scheme 1 shows. The general chemical formula of LDHs could be written as $[M^{2+}_{1-x}\ M^{3+}_{x}(OH)_2](A^{n-})_{x/n}\cdot mH_2O]$, M^{2+} stands for metal ions such as Mg^{2+}, Ni^{2+}, Zn^{2+}, M^{3+} represents trivalent metal ions like Al^{3+}, Cr^{3+}, Fe^{3+}, Sc^{3+}, A^{n-} indicates the anions including CO_3^{2-}, NO_3^-, Cl^-, PO_4^{3-} etc [1–6]. The quantities of the layer metal cations and the anions between the layers are adjustable to bring changes to the layer charge density and other chemical properties, therefore, it could generate useful novel catalytic properties for the LDHs materials. The introduction of Cu, Zn and Ti elements into the LDHs layers would generate active sites such as O—Cu—O, O—Zn—O and O—Ti—O, which would narrow the energy band gap [7–9]. The valence electrons are thus easily excited into the conduction band and generate electron-hole pairs, which would improve the photocatalytic oxidation and reduction activity of those materials. LDHs has been used as an efficient and effective photocatalyst on the organic pollutant degradation reaction, recent years [10–13]. But the researches have been mainly concentrated on the photodegradation of traditional azo dye pollutants which are easier to decomposed [14–17]. Although, the application of LDHs on photodegrading more robust permanent organic pollutants (POPs) has been reported, the photocatalytic activity and pollutants removal were not desirable [18,19]. In addition, several researchers reported the photocatalytic mechanisms and reaction pathways of POPs, but there is a lack of systematic and deep fundamental study [20,21].

Based on the previous study in our group, we found that the metal element (such as Cr, Fe, Ce or Ti) modified LDHs showed the excellent activity on photocatalytic oxidation reaction [22],

* Corresponding authors.
E-mail addresses: xiasj@zjut.edu.cn (S. Xia), jchx@zjut.edu.cn (Z. Ni).

http://dx.doi.org/10.1016/j.apcatb.2017.05.033
0926-3373/

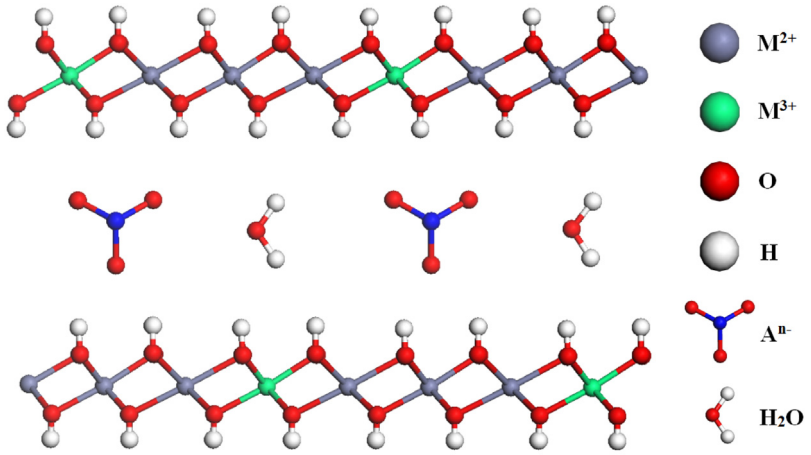

Scheme 1. The structural model of layered double hydroxides (LDHs).

and this activity could be enhanced by introducing metal element metalorganic complex [23,24]. Other researchers reported that the introduction of metal oxides could also improve the reactivity of LDH materials dramatically [25–27]. Therefore, based on the fact that three modifications with different Cu-containing species could all improve the photocatalytic activity of LDHs, the combination of all three different modifications, which could introduce all the three Cu species together into the same type of LDHs material, were proposed. Could such combination modification improve the reactivity even more than just one single modification? Does different Cu-containing species introduced by those three different modifications have the same activity and selectivity during the photocatalytic reaction? Which modification has the most significant effect on the photocatalytic activity?

Based on the assumptions mentioned above, we planned to synthesize a novel LDHs material with different organic/inorganic Cu species. The Cu elements would be distributed in the layers, between the layers and also combined on the surface of the material. The percentages of each species were adjusted to reveal the connection between different modifications and their photocatalytic activities towards the 2,4,6-trichlorophenol photodegradation. Also, the photoreaction mechanism, intermediates and degradation pathway of 2,4,6-trichlorophenol were also investigated in detail.

2. Experimental

2.1. Materials

Copper oxide, 5,5-dimethyl pyridine *n*-oxide (DMPO), dimethyl sulfoxide (DMSO), 2,4,6-trichlorophenol (abbreviated as TCP) were guaranteed reagent (GR) and purchased from Alfa Aesar. Ethanol, formic acid, salicylaldehyde and sodium 4-Aminobenzoate were analytical reagent (AR) and purchased from Aladdin Chemistry Co. Ltd. Copper nitrate, chromic nitrate and others were all purchased from Guoyao Fine Chemical Co. Ltd. In addition, ultrapure water was used and decarbonated by boiling N_2 before employing in all synthetic process.

2.2. Synthesis of Cu^1Cr–LDHs

A typical synthetic procedure is given as follows: under nitrogen atmosphere, an aqueous solution (100 ml) containing NaOH (16.0 g, 0.4 mol) was added dropwise to a solution (150 ml) containing designated amounts of $Cu(NO_3)_2{\cdot}3H_2O$ and $Cr(NO_3)_3{\cdot}9H_2O$ (the mole ratio of Cu/Cr is from 2.0 to 4.0) with vigorous stirring until the final pH = 8.5. The resultant slurry was aged at 85 °C for 18 h, and then, the product was centrifuged and washed thrice with deionized water until the pH = 7. Finally, the sample was dried in vacuo at 65 °C for 18 h. After grounded, the product of CuCr–NO_3–LDHs could be obtained (abbreviated as Cu^1Cr–LDHs, Cu species distributed in the LDH layers were marked as Cu^1). The preparation route for the Cu^1Cr–LDHs is depicted in route A of Scheme 2.

2.3. Synthesis of Cu^1Cr–Cu^2/SB–LDHs

2.3.1. Preparation of Cu/Schiff-base

The synthetic apparatus is shown in Fig. S1. In 250 ml flask, 100 ml of ethanol solution containing 6.12 g (50 mmol) salicylaldehyde was added dropwise into a solution containing 6.86 g (50 mmol) of sodium 4-Aminobenzoate and 50 ml of ethanol with vigorous stirring for 30 min. Then, the reaction system was continuously stirred for 3 h at a refluxing temperature of 85 °C. The resultant slurry was then condensed, refrigerated, filtered, washed with ice-cold ethanol and dissolved with warm ethanol, after repeating the above-mentioned steps three times. Finally, after the product was dried in vacuo oven at 60 °C for 6 h, the sample of Schiff-base ligand could be obtained ($C_{14}H_{10}NO_3Na$, 263 g/mol, abbreviated as SB).

An ethanolic solution (60 ml) containing as-synthesized SB ligand (0.711 g, 2.7 mmol) was added dropwise to a solution containing 0.24 g (1.5 mmol) of $CuSO_4$ and 20 ml of ethanol with vigorous stirring under the N_2 atmosphere. Then, the produced suspension was continued stirred for 2 h at a refluxing temperature of 85 °C. The slurry was filtered, washed thrice with ethanol and recrystalized from diethyl ether. Finally, after it was dried in vacuo oven at 65 °C for 6 h, the product of Cu/Schiff-base complex could be obtained ($(C_{14}H_{10}NO_3Na)_2Cu$, 590.0 g/mol, abbreviated as Cu/SB).

2.3.2. Preparation of CuCr–Cu/Schiff base–LDHs

The synthetic procedure of CuCr–Cu/Schiff-base–LDHs was the same like the ion-exchange method which is given as follows: under nitrogen atmosphere, firstly, 1.5 g dried CuCr–LDHs was added into 50 ml ethanol solution and stirred for 1 h; secondly, designated amounts of Cu/SB complex was transferred into the above mentioned ethanolic suspension of LDH, and the reaction system was refluxed at 80 °C for 24 h with constant stirring; finally, after the product was isolated by filtration and washed with ethanol

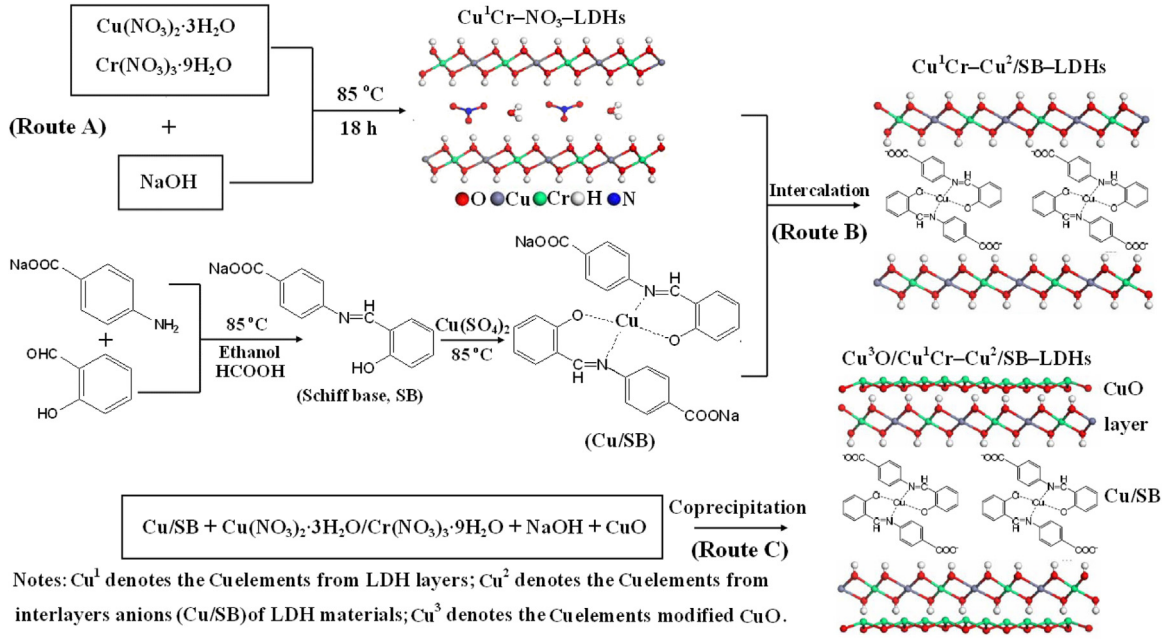

Scheme 2. The complete preparation pathway and structure for three types of multi-copper-contained LDHs based materials.

and kept overnight in vacuum at 65 °C, samples of CuCr–Cu/Schiff-base–LDHs could be obtained (abbreviated as $Cu^1Cr–Cu^2$/SB–LDHs, Cu species distributed between the LDH layers were marked as Cu^2). The complete preparation pathway for $Cu^1Cr–Cu^2$/SB–LDHs is depicted in route B of Scheme 2.

2.4. Synthesis of $Cu^3O/Cu^1Cr–Cu^2$/SB–LDHs

Coprecipitation method can be used to synthesis $Cu^3O/Cu^1Cr–Cu^2$/SB–LDHs: during the synthetic procedure of CuCr–Cu/Schiff-base–LDHs, at the meantime, under nitrogen atmosphere, designated amounts of CuO nanopowder were added into the solution. The subsequent process was similar with the synthesis of CuCr–Cu/Schiff-base–LDHs. Finally, the multi-copper-contained hybrid materials contained three different Cu species, that is $Cu^3O/Cu^1Cr–Cu^2$/SB–LDHs (Cu species distributed on the surface of the LDH based materials were marked as Cu^3), could be obtained. The detailed mole ratios of different Cu species were given in the note of Table 1. The structure of $Cu^3O/Cu^1Cr–Cu^2$/SB–LDHs is shown in route C of Scheme 2.

2.5. Materials characterization

C, H and N elemental microanalyses were obtained on a ThermoFisher Italia S.P.A elemental analyzer; Cu and Cr element analysis was conducted using inductively coupled plasma atomic emission spectrometry (ICP–AES) on a IRIS Intrepid II XSP instrument.

Powder X-ray diffraction (XRD) was recorded on a Rigaku UltimaIV powder diffractometer with the testing of Cu Kα radiation (λ = 1.54 Å) at 40 kV and 178 mA and scanning rate of 5°/min in the range of 5–70°.

SEM–EDS analysis was carried out in a Hitachi SU1510 ESEM with an acceleration voltage of 15 kV. The TEM was recorded on a Hitachi HT-7700 to examine the morphologies, lattice fringes and crystal boundaries of the samples.

The pore structure of the materials was analyzed by N_2 adsorption–desorption at 77 K on a Micromeritics Instrument Corporation ASAP2020 M apparatus. Before the analysis, the samples were degassed in a vacuum at 120 °C for 6 h. The specific surface areas were calculated by the Brunauer–Emmett–Teller (BET) method. The pore size distribution as well as total pore volume were determined by the Brunauer–Joyner–Hallenda (BJH) method.

Solid state UV–vis diffuse reflectance spectra was recorded at room temperature in the air by means of a Shimadzu UV-2600 spectrometer equipped with an integrating sphere attachment. $BaSO_4$ was used as background. The concentrations of TCP and the degradation intermediates were tested by Varian CP-3800/Sature2200 (GC–MS analysis).

Electron spin resonance (ESR) was tested by Bruker A200 ER083CS apparatus. The mixed solution of DMPO and water was used to detect hydroxide radicals; the DMSO solution with no water was used to detect superoxide radicals; the mixed solution of DMSO and water was used to detect peroxide radicals. The trapping reagent was DMPO.

2.6. Photocatalytical degradation of TCP

A 300 W xenon lamp (400 nm < λ < 800 nm) equipped with a constant temperature circulator at 15 °C was used during the photocatalytic degradation of TCP under visible light irradiation. Typically, in 150 ml reactor, a mixture of 100 ml of TCP (1 mg/L) solution and 50 mg of catalyst was stirred with the rate of 300 rpm for 30 min to establish an adsorption/desorption equilibrium in dark. Then the reaction solution was stirred under visible light irradiation for 210 min at 15 °C. At given time intervals, 2 ml aliquots were sampled and filtered to remove the solid phase. The concentration of TCP in filtrate was tested by GC–MS at 290 nm and the blank reaction was also carried out by the same procedure without adding any catalyst.

3. Results and discussion

3.1. Structural characteristics of $Cu^3O/Cu^1Cr–Cu^2$/SB–LDHs

3.1.1. Elementary analysis and X-ray diffraction

On the basis of elementary analysis results (C, H, N from elemental analyzer; Cu, Cr from ICP–AES), the chemical composition of different multi-copper-contained LDH based materials is listed in Table 1. Based on the theoretical structure and chemical com-

Table 1
The chemical composition of multi-copper-contained LDHs based materials.

Sample	Chemical formula	Cu* (wt%)			Cr (wt%)	C (wt%)	H (wt%)	N (wt%)
		Cu^1	Cu^2	Cu^3				
1	$Cu_{0.76}Cr_{0.24}(OH)_2$ $(NO_3^-)_{0.26}$ $0.49H_2O$	40.5 40.5	–	–	10.4	–	2.48	3.03
2	$Cu_{0.74}Cr_{0.26}(OH)_2$ $(Cu/SB)_{0.22}$ $0.48H_2O$	27.5 21.2	6.31	–	6.06	33.1	3.30	2.76
3	$(CuO)_{0.23}Cu_{0.66}Cr_{0.34}(OH)_2$ $(Cu/SB)_{0.22}$ $0.46H_2O$	31.1 17.6	5.86	7.66	7.36	30.8	3.05	2.56
4	$(CuO)_{0.22}Cu_{0.74}Cr_{0.26}(OH)_2$ $(Cu/SB)_{0.21}$ $0.46H_2O$	33.4 20.2	5.72	7.49	5.75	30.0	3.03	2.50
5	$(CuO)_{0.21}Cu_{0.79}Cr_{0.21}(OH)_2$ $(Cu/SB)_{0.19}$ $0.49H_2O$	40.0 22.5	5.42	7.48	4.87	28.4	3.02	2.37
6	$(CuO)_{0.26}Cu_{0.74}Cr_{0.26}(OH)_2$ $(Cu/SB)_{0.13}$ $0.46H_2O$	39.3 24.3	4.27	10.7	6.94	22.4	2.84	1.87
7	$(CuO)_{0.25}Cu_{0.74}Cr_{0.26}(OH)_2$ $(Cu/SB)_{0.29}$ $0.48H_2O$	30.5 16.8	6.60	7.11	4.81	34.6	3.11	2.89
8	$(CuO)_{0.12}Cu_{0.74}Cr_{0.26}(OH)_2$ $(Cu/SB)_{0.22}$ $0.46H_2O$	30.6 20.4	6.06	4.13	5.82	31.8	3.15	2.65
9	$(CuO)_{0.36}Cu_{0.73}Cr_{0.27}(OH)_2$ $(Cu/SB)_{0.22}$ $0.47H_2O$	35.6 18.6	5.59	11.4	5.58	29.4	2.92	2.45

Note: sample 1 is CuCr–NO_3–LDHs; sample 2 is CuCr–Cu/SB–LDHs; samples 3–9 are CuO/CuCr–Cu/SB–LDHs: among the samples 3–5, the content of **Cu^1 is changed** (mole ratios of $Cu^1/Cr = 2, 3, 4$) while Cu^2 and Cu^3 are fixed ($Cu^2/Cu^3 = 1$); among the samples 6, 4 and 7, the content of **Cu^2 is changed** ($Cu^2/Cr = 0.5$, 1, 1.5 and $Cu^1/Cr = 3$) while Cu^1 and Cu^3 are fixed ($Cu^1/Cu^3 = 3$); among the samples 8, 4 and 9, the content of **Cu^3 is changed** ($Cu^3/Cr = 0.5$, 1, 1.5 and $Cu^1/Cr = 3$) while Cu^1 and Cu^2 are fixed ($Cu^1/Cu^2 = 3$). SB is $(C_{14}H_{10}NO_3)_2Cu$, 544.0 g/mol.
Cu* is the total Cu content of sample which is obtained from ICP–AES, Cu^1, Cu^2 and Cu^3 are Cu elements distributed in the layers, between the layers and combined on the surface of the material, respectively.

position of materials, the simplest molecular formula of such LDH based materials is calculated and given in Table 1. It indicates that the structure of synthesized samples is basically agreed with the composition of objective materials.

Fig. 1 shows the XRD patterns of multi-copper-contained LDH based materials. The characteristic peaks of 003, 006, 009, 012, 015, 110 and 113 are all observed in the sample of CuCr–LDHs, which indicates the successful synthesis of typical LDH material (curve *a* in Fig. 1A). As we know the thickness of the LDHs layer is a constant value of 0.48 nm, the gallery height-defined as the layer distance subtracting the layer thickness-would be associated with cation exchange, which means that the gallery height would increase when ions with bigger size replace the nitrite ions, which at the same time would cause the increment of 2θ. The interlayer distance (d_{003}) of CuCr–LDHs is 0.821 nm ($2\theta = 10.8^\circ$), it is consisted with the results reported by other authors [28,29]. For CuCr–Cu/SB–LDHs (curve *b* in Fig. 1A), the typical peaks of LDHs also appear, but, the interlayer distance (d_{003}) increases to 1.08 nm ($2\theta = 8.2^\circ$). The increment of gallery height confirms the successful intercalation of the Cu/SB complex and the formation of organic–inorganic hybrid composite. For CuO/CuCr–Cu/SB–LDH samples (curves *c*–*k* in Fig. 1), one side, they all retain the typical peaks of LDHs, and the interlayer distance (d_{003}) increases to 1.10–1.13 ($2\theta = 8.1$–7.9°); on the other hand, the materials also appear the typical peaks of CuO [30]. It confirms the successful fabrication of multi-copper-contained LDH based materials. Certainly, XRD was just used to qualitatively tell the formation of CuO/CuCr–Cu/SB–LDHs. The schematic illustration for CuCr–NO_3–LDHs (A), CuCr–CuSB–LDHs (B) and CuO/CuCr–CuSB–LDHs (C) was given in Fig. S2.

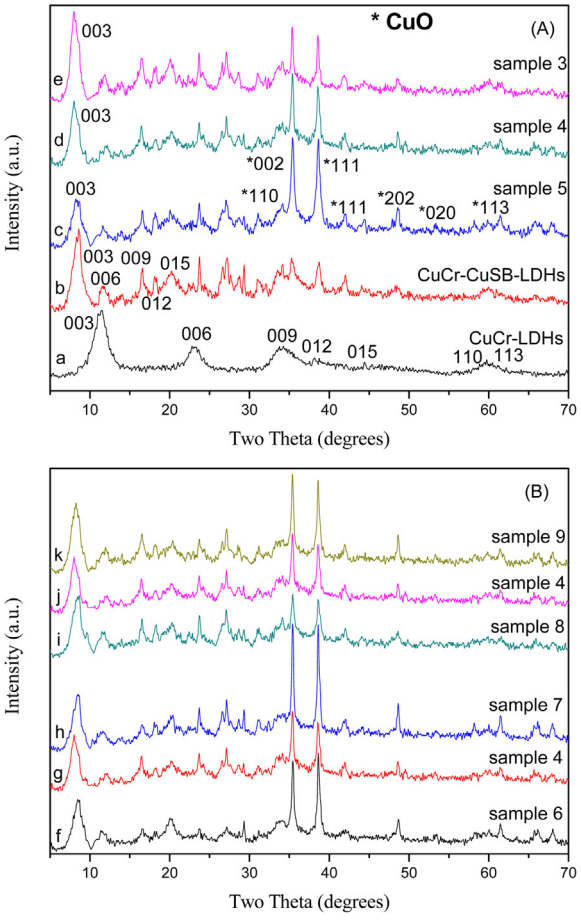

Fig. 1. The XRD curves of multi-copper-contained LDHs based materials: *a* is CuCr–LDHs; *b* is CuCr–CuSB–LDHs; *c*–*k* are CuO/CuCr–CuSB–LDHs.

3.1.2. Specific surface area and pore size distribution

The pore size distribution curves and N_2 adsorption–desorption isotherms for LDHs based materials are shown in Fig. 2. CuCr–LDHs (Fig. 2A) and CuCr–Cu/SB–LDHs (Fig. 2B) are both Type II isotherms due to broad H3 type hysteresis loops. The isotherms also indicate that these two catalysts are mainly macroporous materials. From the pore size distribution curves, it is also partially mesoporous. The isotherm for CuO/CuCr–Cu/SB–LDHs is type IV (because all the isotherms are similar for different CuO/CuCr–Cu/SB–LDHs, Fig. 2C is just sample 4), which is assigned to mesoporous structure, according to the IUPAC classification [31]. Pore size distribution curves and isotherms for all CuO/CuCr–Cu/SB–LDHs samples are some-

Table 2
The band gap energy and textural properties of multi-copper-contained LDHs based materials.

Sample	Surface area (m^2/g)	Pore volume (cm^3/g)	Pore size distribution (nm)	Band gap (eV)
1	100.1	0.529	18, 30, 65	2.91
2	119.8	0.518	16, 30, 60	2.74
3	155.9	0.486	5.0, 18, 60	2.59
4	162.7	0.479	5.0, 16, 55	2.48
5	168.6	0.473	4.8, 16, 55	2.41
6	143.2	0.497	5.5, 20, 60	2.65
7	177.4	0.465	4.6, 15, 52	2.33
8	157.3	0.483	5.0, 16, 60	2.56
9	169.8	0.472	4.8, 15, 55	2.39

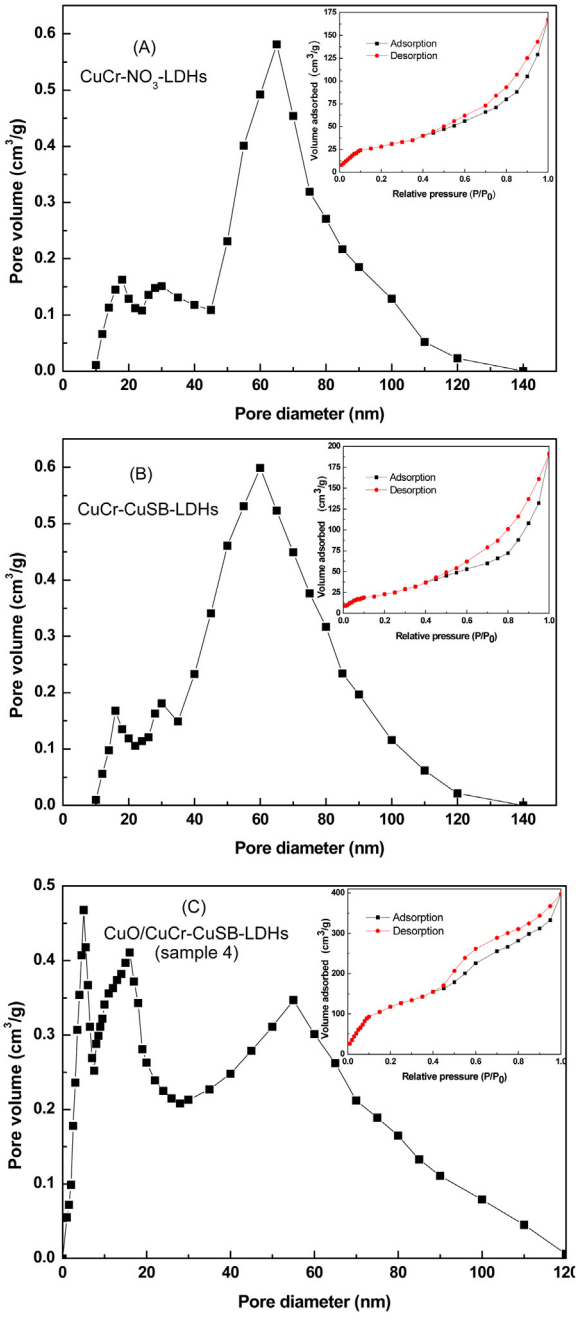

Fig. 2. Pore size distribution and N_2 sorption isotherms for multi-copper-contained LDHs based materials.

what similar, while, there are obvious differences in specific surface area, pore volume and pore size distribution (shown in Table 2). CuO/CuCr–Cu/SB–LDHs show larger surface area and narrower pore size distribution than that of CuCr–LDHs and CuCr–Cu/SB–LDHs. The specific surface area of LDHs increases with the increasing of Cu species in the layers (sample 3, 4, 5), between the layers (sample 6, 4, 7), or combined on the surface (sample 8, 4, 9), respectively. The sample with the highest Cu content between the layers shows the highest specific area and the narrowest pore size distribution, with 177.4 m^2/g and 4.6 nm, 15 nm, 52 nm, respectively.

3.1.3. SEM and ultraviolet–visible spectrophotometer

The SEM image of CuCr–LDHs is shown in Fig. 3A . It can be seen that the material layers pile up together with lamellar crystal type structure. Fig. 3B is the SEM picture of CuCr–Cu/SB–LDHs. The materials modified by schiff base not only show layered structures, but also have regulated rectangular shapes. Fig. 3C shows the SEM of $Cu^3O/Cu^1Cr–Cu^2$/SB–LDHs. As the surface of the $Cu^3O/Cu^1Cr–Cu^2$/SB–LDHs has been modified with CuO nano particles, the layered structure is irregularly distributed and the surface of the materials has attached nano particles. In addition, the EDS curve and quantitative analysis result are given in supporting materials (please see Fig. S3 and Table S1). It can be concluded that the contents of Cu, Cr, C and N elements obtained from EDS is quite consistent with the results of ICP–AES.

Fig. 4 is TEM images of CuCr–LDHs, CuCr–Cu/SB–LDHs and $Cu^3O/Cu^1Cr–Cu^2$/SB–LDHs. As shown in Fig. 4A and 4B, CuCr–LDHs nanoparticles display obvious lamellar crystal with layered structure, and the crystallite size is at the range of 20–100 nm. From Fig. 4C and 4D, we can see that CuCr–Cu/SB–LDHs still retain the layered structure of typical LDHs, and show the diamond-shaped morphology with an average diameter about 100–200 nm. The TEM images of $Cu^3O/Cu^1Cr–Cu^2$/SB–LDHs (Fig. 4E and F) indicate that this multi-copper-contained hybrid material is a composite of CuO and LDHs, and the dark spots of CuO particles are dispersed in random on the surface of LDH particles. The average diameter of those lamellar crystals is about 150–250 nm.

Fig. 5A is the UV-curves for all the multi-copper-contained hybrid materials. We can see that all 9 different kinds of LDHs based samples have a strong and broad adsorption peak at 400–800 nm, especially for sample 2–9, which is in the visible light region. Compared to the CuCr–LDHs (sample 1) and CuCr–Cu/SB–LDHs (sample 2), all of the multi-copper-contained hybrid materials (sample 3–9) show obvious red shifts, which would increase the absorption range of the material and improve the performance of the material in visible light region. We also plotted the photon energy against the $(\alpha hv)^2$ based on the adsorption efficiency, and calculated the band gap based on the intercept of the fit curve (please see Fig. 5B and Table 2). The band gap of CuO/CuCr–Cu/SB–LDHs is at the range of 2.33–2.65 eV, which is narrower than that of CuCr–LDHs (2.91 eV) and CuCr–Cu/SB–LDHs (2.73 eV). It indicates that CuO/CuCr–Cu/SB–LDHs has higher utilization ratio of visible light than that of CuCr–LDHs and CuCr–Cu/SB–LDHs.

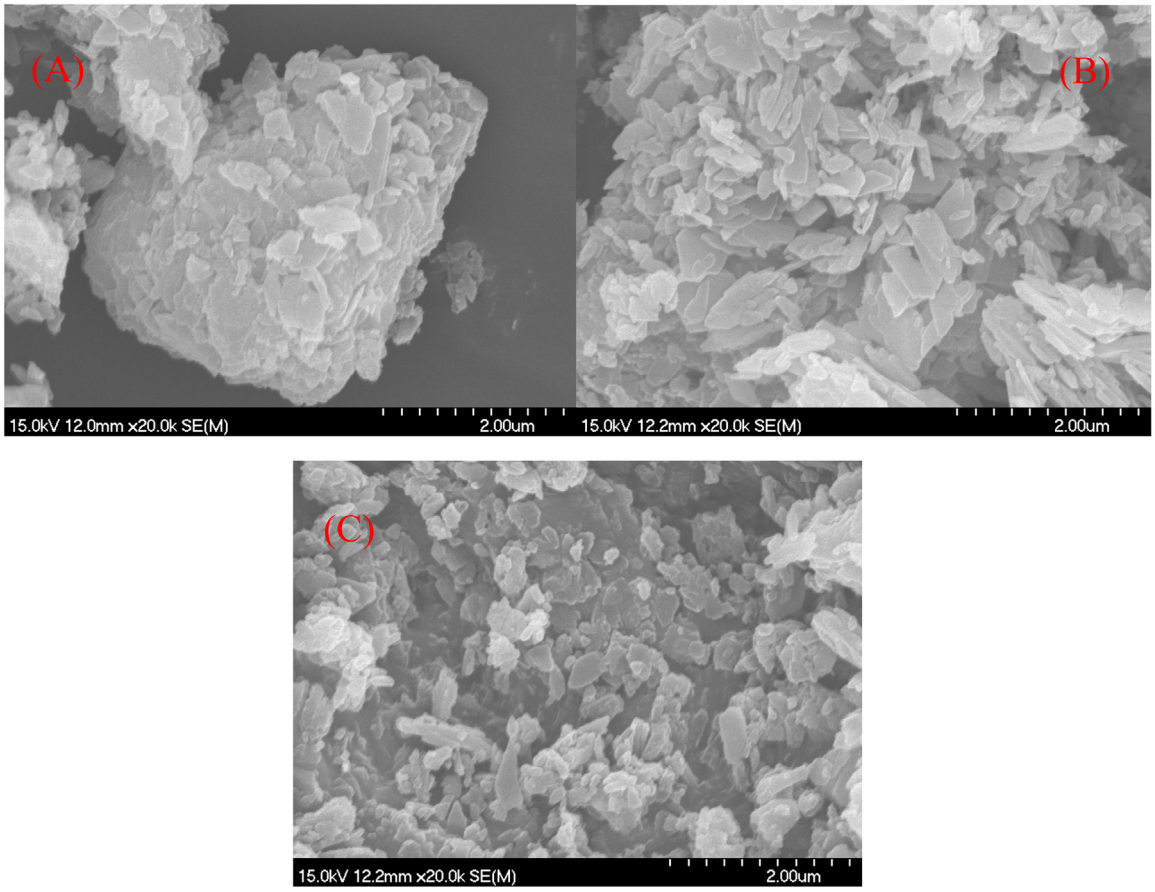

Fig. 3. SEM images for (A) CuCr–LDHs, (B) CuCr–Cu/SB–LDHs, (C) CuO/CuCr–Cu/SB–LDHs (sample 4).

3.2. The influence of different Cu species onto the multi-copper-contained hybrid materials' photocatalytic property

3.2.1. The photocatalytic degradation of TCP

Fig. 6A displays the removal rate of TCP by different samples under visible light irradiation (the reaction reached equilibrium after 180 min). As the figure tells, TCP removal rate of all three Cu containing $Cu^3O/Cu^1Cr–Cu^2$/SB–LDHs is between 72.9%–95.1%, which is dramatically increased, compared to the 44.5% of ZnCr–LDHs (sample 1) and 62.6% of CuCr–Cu/SB–LDHs (sample 2). In addition, the photocatalytic performance will increase with the increasing of Cu% in metal layer, intercalating layer and also at the material surface. The biggest factor to improve the activity is the amount of Cu between the layers, as we can see that the removal rates of TCP for sample 6, 4 and 7 are 72.9%, 83.4% and 95.1%. In addition, TCP removal efficiency is compared among the different photocatalysts under visible light irradiation, the results was given in Table S2. It indicates that the TCP removal efficiency for $Cu^3O/Cu^1Cr–Cu^2$/SB–LDHs (sample 7) is 0.64 mg/g h, which is higher than that of many reported photocatalytic systems (0.28–0.79 mg/g h) [32–37].

Furthermore, the apparent quantum efficiencies according to the total optical power impinging on the samples for degradation of HCB were calculated by the following equation:

$$\varphi_x = \frac{\pm(d[x]/dt)}{d[hv]_{inc}/dt}$$

where d[x]/dt is the change rate of the concentration of the targeted contaminant and $d[hv]_{inc}/dt$ is the total optical power impinging on the reaction liquid [38]. The result is shown in Fig. 6B, from which we can see that the apparent quantum efficiency of different $Cu^3O/Cu^1Cr–Cu^2$/SB–LDH materials (sample 3–9) is at the range of 0.42% to 0.60%, which is higher than that of CuCr–LDHs (sample 1, 0.21%) and CuCr–CuSB–LDHs (sample 2, 0.32%).

3.2.2. The analysis of active free radicals

ESR technique was used to determine the active free radicals and to explain the reaction mechanism of $Cu^3O/Cu^1Cr–Cu^2$/SB–LDHs during the photocatalytic degradation of TCP. 5,5-Dimethyl pyridine *n*-oxide (DMPO) was used as a trapping agent for free radicals. The results are shown in Fig. 7. As we can see, there is no radical for $Cu^3O/Cu^1Cr–Cu^2$/SB–LDHs under dark condition, while, it shows typical intense peaks of DMPO–$^{\bullet}$OH (hydroxide radicals) and overlapping small peaks for DMPO–$^{\bullet}O_2^-$ (superoxide radicals) and DMPO–$^{\bullet}$OOH (peroxide radicals) when material is exposed under visible light. This result indicates that the oxidation reaction is possibly gone through $^{\bullet}$OH radicals as well as $^{\bullet}O_2^-$ radicals and $^{\bullet}$OOH radicals.

To further study the relevance of the Cu species with the reaction mechanism of the free radicals, we used ESR to study the 3 different free radicals after 30 min of the TCP photocatalytic reaction. The results are posted in Figs. S4–S9. Figs. S4 and S5 are the DMPO–$^{\bullet}$OH spectrum and the corresponded ESR signal intensity, in which the sample 7 has the strongest peak among all materials which indicates that it generated the most OH radicals during the reaction. For sample 6, 4 and 7, the amount of hydroxyl radicals increases with the increasing of Cu% between the layers, which is a strong sign that Cu^2 species have large influences on the generation of OH radicals. Figs. S6–S7 are the DMPO–$^{\bullet}O_2^-$ spectrum and the corresponded ESR signal intensity, in which the sample 5 has the strongest peak among all materials which indicates that it generated the most $^{\bullet}O_2^-$ radicals during the reaction. For sample 3, 4

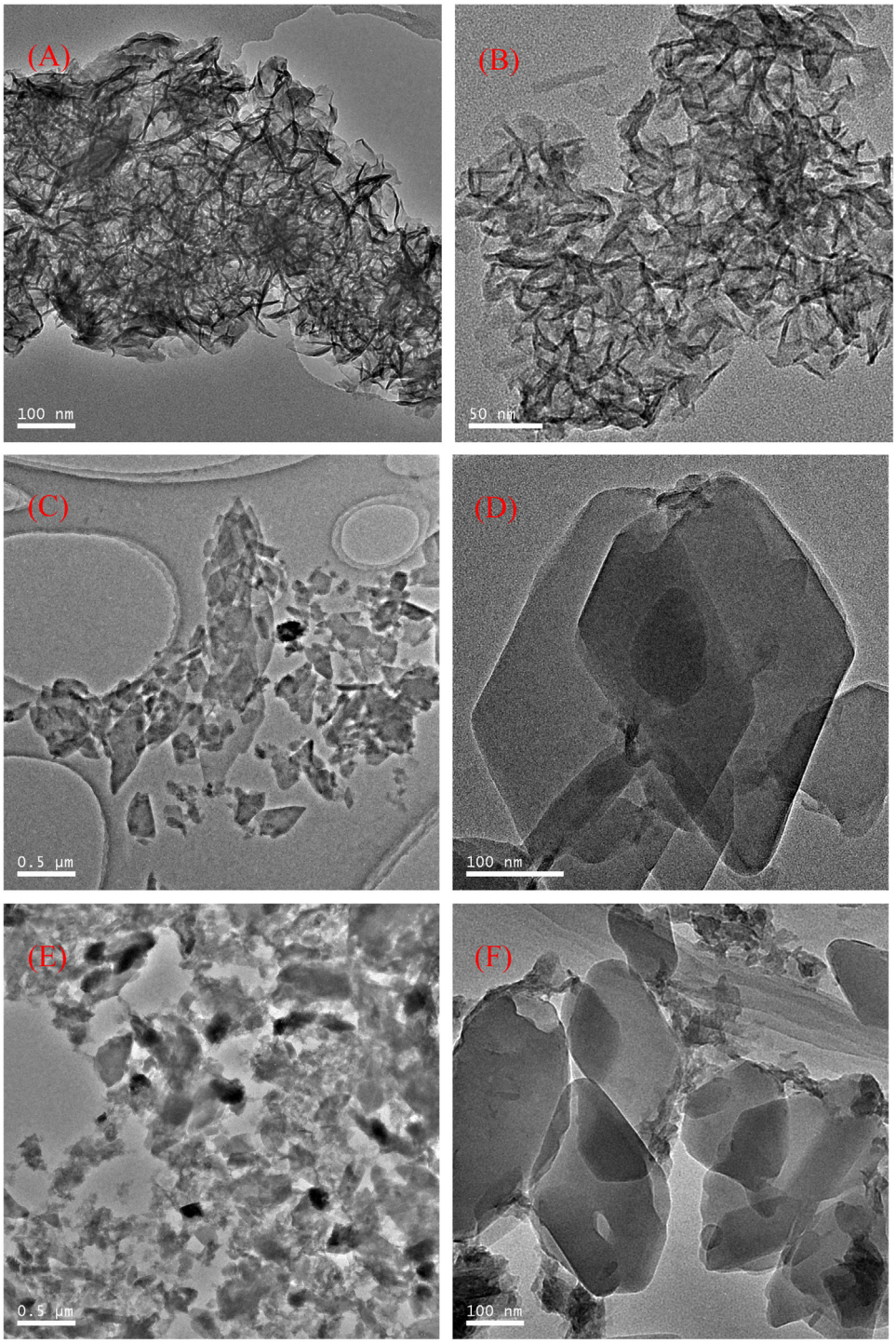

Fig. 4. TEM images for CuCr–LDHs with middle– (A) and high–magnification (B), CuCr–Cu/SB–LDHs with low– (C) and middle–magnification (D), CuO/CuCr–Cu/SB–LDHs (sample 4) with low– (E) and middle–magnification (F).

and 5, the amount of $^{\bullet}O_2^-$ radicals increase with the increasing of Cu% in the LDHs layer, which indicates that Cu^1 species have large influences on the generation of $^{\bullet}O_2^-$ radicals. Figs. S8–S9 are the DMPO–$^{\bullet}$OOH spectrum and its ESR peak intensity. Sample 9 has the strongest DMPO–$^{\bullet}$OOH peak intensity which reveals that this material produced the highest amount of $^{\bullet}$OOH radicals during the reaction. In this case, surface modified Cu% shows the same influence on the $^{\bullet}$OOH radicals–the higher the Cu^3 content, the higher concentration of $^{\bullet}$OOH generated (see samples 8, 4, 9).

Based on above mentioned analysis, we can make the following conclusions that Cu distributed in the layers determines the production of superoxide radicals, Cu intercalated into the layers determines the generation of hydroxide radicals, and the Cu combined on the LDHs surface is responsible for the production of peroxide radicals.

To further study the roles played by different radicals during the $Cu^3O/Cu^1Cr–Cu^2$/SB–LDHs catalytic reaction, we designed the experiment to trace the active site. DMPO was used to capture hydroxide radicals, superoxide radicals and peroxide radicals under

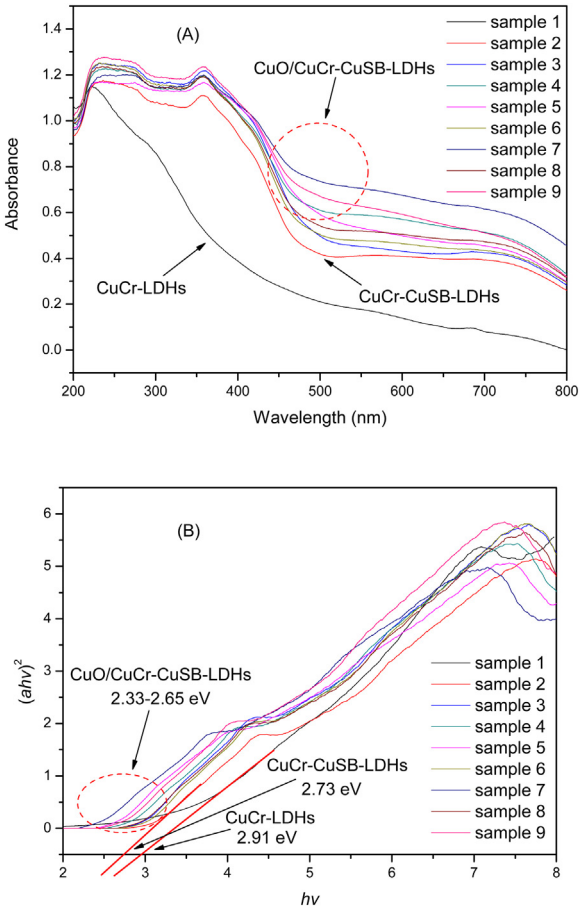

Fig. 5. The UV–vis curves (A) and plots of hv vs $(\alpha hv)^2$ (B) for multi-copper-contained LDHs based materials.

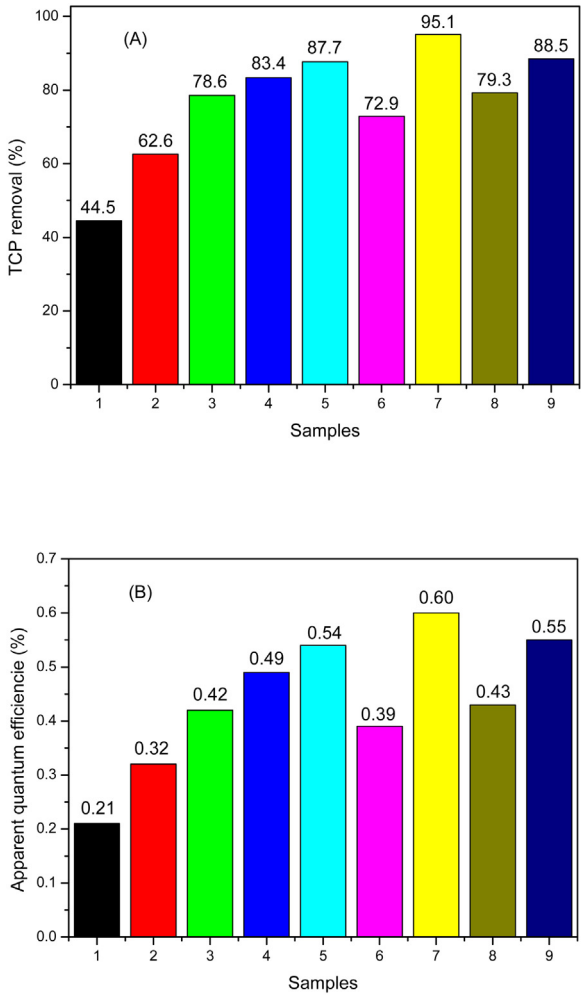

Fig. 6. The photodegradation efficiency of HCB (A) and the apparent quantum efficiencies (B) of different samples under visible light irradiation.

the different reaction conditions of solution and water content. Fig. 8 is the photocatalytic reaction result using sample 3 as the model catalyst. We can see that when OH radicals are fully captured, TCP degradation rate drops from the initial 95.1% to 48.9%, the removal rates are decreased to 72.6% and 84.2% when $^{\bullet}O_2^-$ and •OOH radicals are completely captured respectively as well. We can deduct from this information that the contribution of OH radicals, $^{\bullet}O_2^-$ radicals and •OOH radicals are 46.2% (95.1%–48.9%), 22.5% (95.1%–72.6%) and 10.9% (95.1%–84.2%), respectively. This is also consistent with our ESR measurement of the percentage for these radicals as Fig. 6 shows. The rest of the 15.5% (95.1%–46.2%–22.5%–10.9%) might be from the catalytic reactivity of the electron–hole pairs.

3.3. The intermediates and pathway of TCP degradation photocatalyzed by $Cu^3O/Cu^1Cr–Cu^2/SB–LDHs$

The product was sampled during the reaction and was analyzed by GC–MS after being processed to determine possible intermediates during the reaction. The GC curves and mass spectrum are shown in Fig. S10 and S11 . During the reaction catalyzed by $Cu^3O/Cu^1Cr–Cu^2/SB–LDHs$, the intermediate includes 2,4-dichlorophenol (2), 2,6-dichlorophenol (3), 4-chlorophenol (4) and phenol (5) which are from the dechlorinating reaction; 2,3,4,6-tetrachlorophenol (6), dibenzofuran (7), and small organic acids (oxalic acid (8) and caproic acid (9)).

Based on GC–MS results and referencing the information from other authors [39–42], we concluded the degradation mechanism

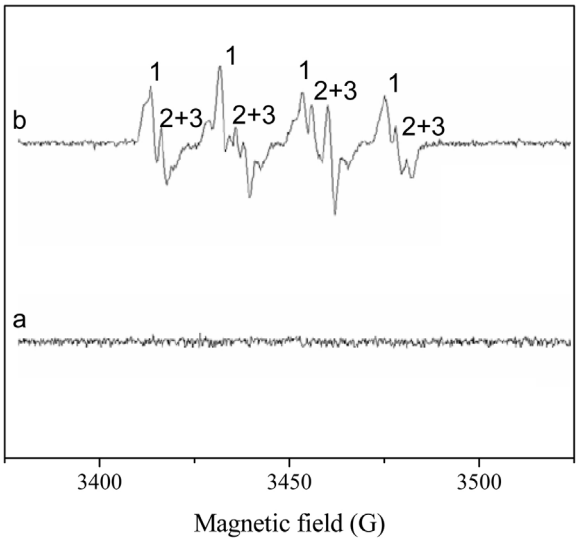

Fig. 7. The ESR spectrum of $Cu^3O/Cu^1Cr–Cu^2/SB–LDHs$ (curve *a* for dark, *b* for visible light irradiation).
Note: 1. DMPO–•OH; 2. DMPO–$^{\bullet}O_2^-$; 3. DMPO–•OOH.

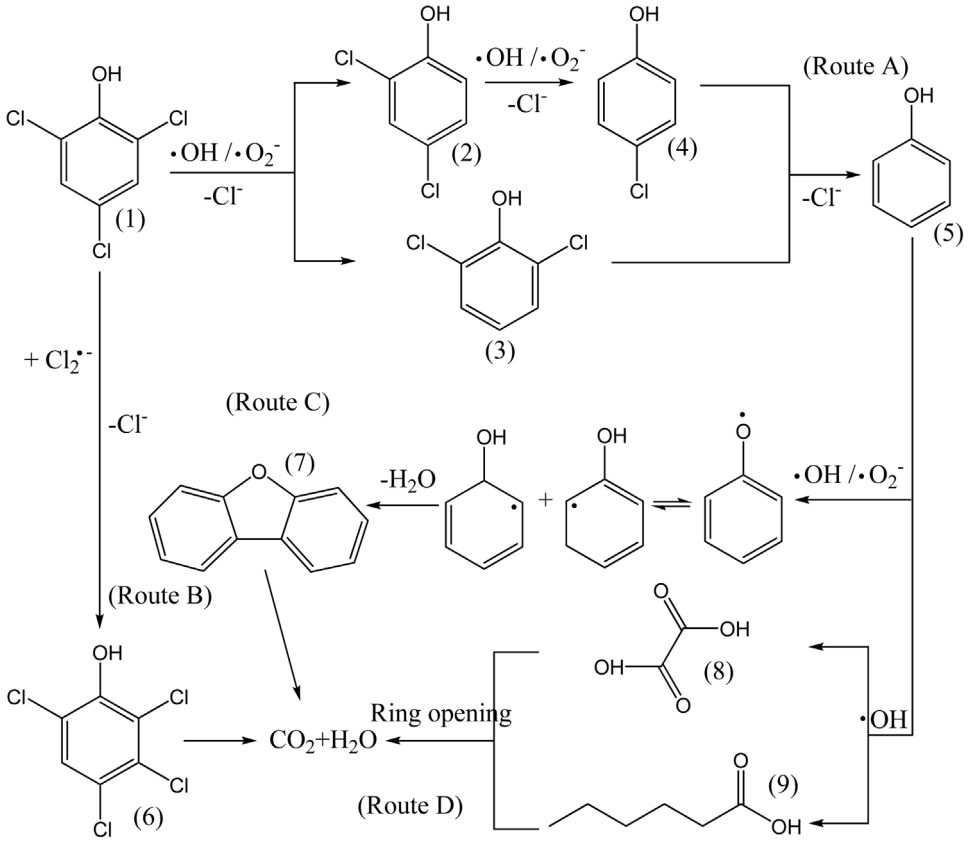

Scheme 3. The intermediates and degradation pathway of TCP.

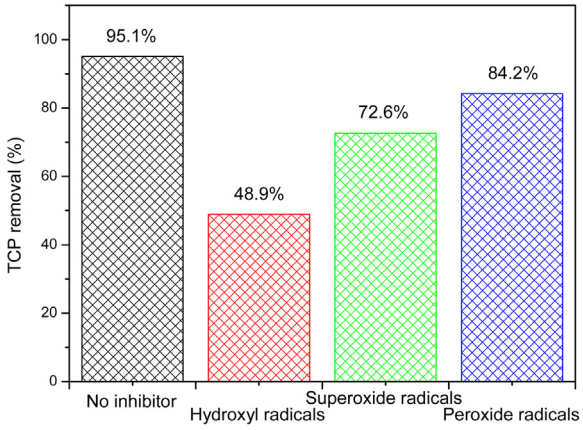

Fig. 8. The trapping experimental results for different free radicals (sample 7).

of 2,4,6-TCP catalyzed by $Cu^{3}O/Cu^{1}Cr–Cu^{2}$/SB–LDHs, as Scheme 3 represents.

(1) Step by step dechloronation reaction

Based on the previous analysis, OH radicals and $^{\bullet}O_2^-$ radicals are the major products to activate the degradation reaction. Therefore, we assume that these two radicals would attack the benzene ring of chlorophenol by going through cycloaddition, and followed by dechloronation by electron transfer to produce 2,4-dichlorophenol, 2,6-dichlorophenol, 4-chlorophenol and phenol, as the route A in Scheme 3 describes.

(2) Chloro-transfer on benzene ring

It is reported that Cl^- can react with OH radicals to form lower oxidant $Cl_2^{\bullet-}$ to participate the photodegradation reaction:

$$^{\bullet}OH + Cl^- = ClOH^{\bullet-}$$
$$ClOH^{\bullet-} + H^+ = Cl^{\bullet} + H_2O$$
$$ClOH^{\bullet-} + Cl^- = Cl_2^{\bullet-} + OH^-$$
$$Cl^{\bullet} + Cl^- = Cl_2^{\bullet-}$$

Therefore, we infer that Cl atom is oxidized by hydroxyl radical to $Cl_2^{\bullet-}$, which attacks the benzene ring to generate 2,3,4,6-tetrachlorophenol and finish the transition of Cl between the rings. This is summarized in route B.

(3) The formation of dibenzofuran

2,4,6-TCP finally becomes phenol after removing chloride step by step, hydrogen is removed from phenol under $OH/^{\bullet}O_2^-$ condition to form phenol intermediate radicals, which lose H_2O by going through elimination reaction, as Scheme 3 route C shows.

(4) Ring opening reaction

2,4,6-TCP finally forms phenol by losing chloride step by step, and the benzene ring is opened under $OH/^{\bullet}O_2^-$ condition, which further degrades into oxalic acid and caproic acid and finally forms small inorganic molecules such as CO_2 and H_2O, as route D shows.

4. Conclusions

Firstly, we synthesized a type of novel multi-copper-contained LDHs materials with Cu species distributed in the layers, between the layers and combined on the surface of the material. These materials showed well crystal structures, large surface areas, narrow pore size distributions and narrow band gaps.

Secondly, TCP photodegradation experiments showed that the photocatalytic performance would increase with the increasing of Cu% in metal layers, interlayers and on the surface of the mate-

rial. The biggest factor to improve the activity was the amount of Cu between the layers (Cu^2). The removal rate of TCP for sample 7 was 95.1%, which was the highest among all the samples. $Cu^3O/Cu^1Cr–Cu^2$/SB–LDHs also exhibited higher photocatalytic performance than most of reported catalysts.

Furthermore, the radical testing experiments indicated that Cu species distributed in the layers (Cu^1) determined the production of superoxide radicals, Cu intercalated into the layers (Cu^2) determined the generation of hydroxide radicals, and the Cu combined on the LDHs surface (Cu^3) was responsible for the generation of peroxide radicals. In addition, during the photocatalytic process, the contributions of OH radicals, $•O_2^-$ radicals and •OOH radicals were 46.2%, 22.5% and 10.9%, respectively.

Finally, GC–MS results showed that the reaction photocatalyzed by $Cu^3O/Cu^1Cr–Cu^2$/SB–LDHs included four steps: step by step dechloronation reaction, chloro-transfer on benzene ring, the formation of dibenzofuran, and ring opening reaction. The intermediates were 2,4-dichlorophenol, 2,6-dichlorophenol, 4-chlorophenol, phenol, 2,3,4,6-tetrachlorophenol, dibenzofuran, and small organic acids (oxalic acid and caproic acid).

Acknowledgments

This work is supported by National Natural Science Foundation of China (21503188) and Zhejiang Provincial Natural Science Foundation of China (LQ15B030002).

Appendix A. Supplementary data

Supplementary data associated with this article can be found, in the online version, at http://dx.doi.org/10.1016/j.apcatb.2017.05.033.

References

[1] G.B.B. Varadwaj, V.O. Nyamori, Layered double hydroxide and graphene-based hierarchical nanocomposites: synthetic strategies and promising applications in energy conversion and conservation, Nano Res. 9 (2016) 3598–3621.
[2] L. Han, S.J. Dong, E.K. Wang, Transition metal (Co Ni, and Fe) based electrocatalysts for the water oxidation reaction, Adv. Mater. 28 (2016) 9266–9291.
[3] F.L. Theiss, G.A. Ayoko, R.L. Frost, Synthesis of layered double hydroxides containing Mg^{2+}, Zn^{2+}, Ca^{2+} and Al^{3+} layer cations by co?precipitation methods–a review, Appl. Surf. Sci. 383 (2016) 200–213.
[4] L. Mohapatra, K. Parida, A review on the recent progress, challenges and perspective of layered double hydroxides as promising photocatalysts, J. Mater. Chem. A 4 (2016) 10744–10766.
[5] G. Abellan, C. Marti-Gastaldo, A. Ribera, E. Coronado, Hybrid materials based on magnetic layered double hydroxides: a molecular perspective, Acc. Chem. Res. 48 (2015) 1601–1611.
[6] G.L. Fan, F. Li, D.G. Evans, X. Duan, Catalytic applications of layered double hydroxides: recent advances and perspectives, Chem. Soc. Rev. 43 (2014) 7040–7066.
[7] M. Morikawa, N. Ahmed, Y. Yoshida, Y. Izumi, Photoconversion of carbon dioxide in zinc–copper–gallium layered double hydroxides: the kinetics to hydrogen carbonate and further to CO/methanol, Appl. Catal. B 144 (2014) 561–569.
[8] P. Gao, F. Li, H.J. Zhan, N. Zhao, F.K. Xiao, W. Wei, L.S. Zhong, H. Wang, Y.H. Sun, Influence of Zr on the performance of Cu/Zn/Al/Zr catalysts via hydrotalcite-like precursors for CO_2 hydrogenation to methanol, J. Catal. 298 (2013) 51–60.
[9] N.T.K. Phuong, M.W. Beak, B.T. Huy, Y.I. Lee, Adsorption and photodegradation kinetics of herbicide 2,4,5-trichlorophenoxyacetic acid with MgFeTi layered double hydroxides, Chemosphere 146 (2016) 51–59.
[10] C. Ma, F.H. Wang, C. Zhang, Z.G. Yu, J.J. Wei, Z.Z. Yang, Y.Q. Li, Z.H. Li, M.Y. Zhu, L.Q. Shen, Photocatalytic decomposition of Congo red under visible light irradiation using MgZnCr–TiO_2 layered double hydroxide, Chemosphere 168 (2017) 80–90.
[11] E.M. Seftel, M.C. Puscasu, M. Mertens, P. Cool, G. Carja, Fabrication of CeO_2/LDHs self-assemblies with enhanced photocatalytic performance: a case study on ZnSn–LDH matrix, Appl. Catal. B 164 (2015) 251–260.
[12] X. Liu, X.F. Zhao, Y. Zhu, F.Z. Zhang, Experimental and theoretical investigation into the elimination of organic pollutants from solution by layered double hydroxides, Appl. Catal. B 140 (2013) 241–248.
[13] L. Mohapatra, K. Parida, M. Satpathy, Molybdate/tungstate intercalated oxo-bridged Zn/Y LDH for solar light induced photodegradation of organic pollutants, J. Phys. Chem. C 116 (2012) 13063–13070.
[14] S. Sansuk, S. Srijaranai, A new approach for removing anionic organic dyes from wastewater based on electrostatically driven assembly, Environ. Sci. Technol. 50 (2016) 6477–6484.
[15] Q.Q. Zhou, F.F. Chen, W. Wu, R. Bu, W. Li, F. Yang, Reactive orange 5 removal from aqueous solution using hydroxyl ammonium ionic liquids/layered double hydroxides intercalation composites, Chem. Eng. J. 285 (2016) 198–206.
[16] M.N. Pahalagedara, M. Samaraweera, S. Dharmarathna, C.H. Kuo, L.R. Pahalagedara, J.A. Gascon, S.L. Suib, Removal of azo dyes: intercalation into sonochemically synthesized NiAl layered double hydroxide, J. Phys. Chem. C 118 (2014) 17801–17809.
[17] K.M. Parida, L. Mohapatra, Carbonate intercalated Zn/Fe layered double hydroxide: a novel photocatalyst for the enhanced photo degradation of azo dyes, Chem. Eng. J. 179 (2012) 131–139.
[18] L. Fernandez, I. Ledezma, C. Borras, L.A. Martinez, H. Carrero, Horseradish peroxidase modified electrode based on a film of Co–Al layered double hydroxide modified with sodium dodecylbenzenesulfonate for determination of 2-chlorophenol, Sensor. Actuat. B. Chem. 182 (2013) 625–632.
[19] G. Morales-Mendoza, F. Tzompantzi, C. Garcia-Mendoza, R. Lopez, V. DelaLuz, S.W. Lee, T.H. Kim, R. Martinez, Mn-doped Zn/Al layered double hydroxides as photocatalysts for the 4-chlorophenol photodegradation, Appl. Clay. Sci. 118 (2015) 38–47.
[20] W.F. Chen, L. Pan, L.F. Chen, Q. Wang, C.C. Yan, Dechlorination of hexachlorobenzene by nano zero-valent iron/activated carbon composite: iron loading, kinetics and pathway, RSC Adv. 4 (2014) 46689–46696.
[21] G.J. Su, Y.X. Liu, L.Y. Huang, Y.L. Shi, A.Q. Zhang, L.X. Zhang, W.B. Liu, L.R. Gao, M.H. Zheng, Synergetic effect of alkaline earth metal oxides and iron oxides on the degradation of hexachlorobenzene and its degradation pathway, Chemosphere 90 (2013) 103–111.
[22] S.J. Xia, L.Y. Zhang, X.B. Zhou, G.X. Pan, Z.M. Ni, The photocatalytic property for water splitting and the structural stability of CuMgM layered double hydroxides (M = Al, Cr Fe, Ce), Appl. Clay Sci. 114 (2015) 577–585.
[23] S.J. Xia, F.X. Liu, Z.M. Ni, W. Shi, J.L. Xue, P.P. Qian, Ti–based layered double hydroxides: efficient photocatalysts for azo dyes degradation under visible light, Appl. Catal. B 144 (2014) 570–579.
[24] S.J. Xia, M.M. Shao, X.B. Zhou, G.X. Pan, Z.M. Ni, Ti/ZnO–M_xO_y composite (M = Al, Cr, Fe, Ce): synthesis, characterization and application as a highly efficient photocatalyst for hexachlorobenzene degradation, Phys. Chem. Chem. Phys. 17 (2015) 26690–26702.
[25] F.R. Zhang, Y.W. Song, S. Song, R.J. Zhang, W.G. Hou, Synthesis of magnetite-graphene oxide-layered double hydroxide composites and applications for the removal of Pb(II) and 2,4-dichlorophenoxyacetic acid from aqueous solutions, ACS Appl. Mater. Interfaces 7 (2015) 7251–7263.
[26] Q.S. Guo, Q.H. Zhang, H.Z. Wang, Z.F. Liu, Z. Zhao, Core–shell structured ZnO@Cu?Zn?Al layered double hydroxides with enhanced photocatalytic efficiency for CO_2 reduction, Catal. Commun. 77 (2016) 118–122.
[27] X.Y. Liang, X.Z. Yang, G.J. Gao, C.F. Li, Y.Y. Li, W.D. Zhang, X.T. Chen, Y.B. Zhang, B.B. Zhang, Y.Q. Lei, Performance and mechanism of CuO/CuZnAl hydrotalcites–ZnO for photocatalytic selective oxidation of gaseous methanol to methyl formate at ambient temperature, J. Catal. 339 (2016) 68–76.
[28] K. Parida, L. Mohapatra, N. Baliarsingh, Effect of Co^{2+} substitution in the framework of carbonate intercalated Cu/Cr LDH on structural electronic, optical, and photocatalytic properties, J. Phys. Chem. C 116 (2012) 22417–22424.
[29] G.R. Williams, A. Clout, J.C. Burley, A kinetic and mechanistic study into the formation of the Cu–Cr layered double hydroxide, Phys. Chem. Chem. Phys. 15 (2013) 8616–8628.
[30] Z.H. Li, M.F. Shao, L. Zhou, R.K. Zhang, C. Zhang, J.B. Han, M. Wei, D.G. Evans, X. Duan, A flexible all-solid-state micro-supercapacitor based on hierarchical CuO@layered double hydroxide core?shell nanoarrays, Nano Energy 20 (2016) 294–304.
[31] F. Al-Wadaani, E.F. Kozhevnikova, I.V. Kozhevnikov, Pd supported on Zn^{II}–Cr^{III} mixed oxide as a catalyst for one-step synthesis of methyl isobutyl ketone, J. Catal. 257 (2008) 199–205.
[32] M.V. Carevic, N.D. Abazovic, T.B. Novakovic, V.B. Pavlovic, M.I. Comor, Zirconium dioxide nanopowders with incorporated Si^{4+} ions as efficient photocatalyst for degradation of trichlorophenol using simulated solar light, Appl. Catal. B 195 (2016) 112–120.
[33] X.F. Hu, H.H. Ji, F. Chang, Y.M. Luo, Simultaneous photocatalytic Cr(VI) reduction and 2,4,6-TCP oxidation over g-C_3N_4 under visible light irradiation, Catal. Today 224 (2014) 34–40.
[34] M.Q. Hu, Y.M. Xu, Visible light induced degradation of chlorophenols in the presence of H_2O_2 and iron substituted polyoxotungstate, Chem. Eng. J. 246 (2014) 299–305.
[35] D. Ma, J. Wu, M.C. Gao, Y.J. Xin, T.J. Ma, Y.Y. Sun, Fabrication of Z-scheme g-C_3N_4/RGO/Bi_2WO_6 photocatalyst with enhanced visible-light photocatalytic activity, Chem. Eng. J. 290 (2016) 136–146.
[36] H. Peng, J. Cui, H.J. Zhan, X. Zhang, Improved photodegradation and detoxification of 2,4,6-trichlorophenol by lanthanum doped magnetic TiO_2, Chem. Eng. J. 264 (2015) 316–321.
[37] A. Jawad, X.Y. Lu, Z.Q. Chen, G.C. Yin, Degradation of chlorophenols by supported Co–Mg–Al layered double hydrotalcite with bicarbonate activated hydrogen peroxide, J. Phys. Chem. A 118 (2014) 10028–10035.

[38] J.M. Buriak, P.V. Kamat, K.S. Schanze, Best practices for reporting on heterogeneous photocatalysis, ACS Appl. Mater. Interfaces 6 (2014) 11815–11816.
[39] M.Q. Hu, Y. Wang, Z.G. Xiong, D.Q. Bi, Y.H. Zhang, Y.M. Xu, Iodine-sensitized degradation of 2,4,6-trichlorophenol under visible light, Environ. Sci. Technol. 46 (2012) 9005–9011.
[40] Y.B. Wang, Y.N. Zhang, G.H. Zhao, H.Y. Tian, H.J. Shi, T.C. Zhou, Design of a novel Cu_2O/TiO_2/carbon aerogel electrode and its efficient electrosorption-assisted visible light photocatalytic degradation of 2,4,6-trichlorophenol, ACS. Appl. Mater. Inter. 4 (2012) 3965–3972.
[41] J.E. Grebel, J.J. Pignatello, W.A. Mitch, Effect of halide ions and carbonates on organic contaminant degradation by hydroxyl radical-based advanced oxidation processes in saline waters, Environ. Sci. Technol. 44 (2010) 6822–6828.
[42] H.H. Ji, F. Chang, X.F. Hu, W. Qin, J.W. Shen, Photocatalytic degradation of 2,4,6-trichlorophenol over g-C_3N_4 under visible light irradiation, Chem. Eng. J. 218 (2013) 183–190.